



HAL
open science

Designing highly luminescent nanocrystals embedded bulk single crystals for X-ray scintillators

Y. Xu, X. Li, M. Xia, Xianghua Zhang

► **To cite this version:**

Y. Xu, X. Li, M. Xia, Xianghua Zhang. Designing highly luminescent nanocrystals embedded bulk single crystals for X-ray scintillators. *Journal of Luminescence*, 2022, 248, pp.118924. 10.1016/j.jlumin.2022.118924 . hal-03691390

HAL Id: hal-03691390

<https://hal.science/hal-03691390>

Submitted on 13 Mar 2023

HAL is a multi-disciplinary open access archive for the deposit and dissemination of scientific research documents, whether they are published or not. The documents may come from teaching and research institutions in France or abroad, or from public or private research centers.

L'archive ouverte pluridisciplinaire **HAL**, est destinée au dépôt et à la diffusion de documents scientifiques de niveau recherche, publiés ou non, émanant des établissements d'enseignement et de recherche français ou étrangers, des laboratoires publics ou privés.

Designing highly luminescent nanocrystals embedded bulk single crystals for X-ray scintillators

Yinsheng Xu¹, Xiaoxi Li,² Mengling Xia,^{3,*} and Xianghua Zhang^{1,3}

[†]State Key Laboratory of Silicate Materials for Architectures, Wuhan University of Technology, Wuhan, Hubei 430074, China

[‡]Wuhan National Laboratory for Optoelectronics (WNLO), Huazhong University of Science and Technology (HUST), Wuhan, Hubei 430074, China.

[¶]Laboratoire des Verres et Céramiques, UMR-CNRS 6226 "Institut des Sciences chimiques de Rennes", Université de Rennes 1, Rennes, 35042, France

Abstract: Metal halide perovskite nanocrystals (PNCs) have demonstrated intense luminescence and short emission lifetime, which perfectly match the requirements of X-ray fast scintillators. However, the poor stability of PNCs restricts their applications. Herein, CsPbBr₃ NCs in a wide band-gap Cs₄PbBr₆ perovskite single crystal (PSC) matrix for efficient light extraction is reported. Benefitting from the protection of the PSC matrix and the perfect lattice matching, the PNCs embedded PSC show highly minimized nonradiative recombination and greatly improved stability. Moreover, by controlling the chemical equilibrium, the self-absorption of PNCs is reduced and the quantum yield increased to 78.5%. Furthermore, the PNCs embedded PSC demonstrates an appreciable light yield of 15,290 photons MeV⁻¹, much higher than the commercial scintillator BGO (8,200 photons MeV⁻¹), and a decay time of 12.8 ns, significantly shorter than almost all the representative scintillators. This work demonstrates unambiguously the potential of PNCs embedded PSC for next-generation fast scintillators.

Keywords: CsPbBr₃ nanocrystals, Cs₄PbBr₆ crystals, scintillators, stability

1 Introduction

Scintillators, which can detect highly ionizing radiation, have been broadly used in space exploration, medical diagnostics and security inspection.[1-3] Light yield, time profile and stability are the most important factors

to be considered for practical applications.[4, 5] For a fast scintillator, short decay time is required, particularly for positron emission tomography (PET), gamma-ray/particle discrimination via time-of-flight techniques and some security inspection systems or nuclear physics when timing resolution is important. Commercial activator-doped scintillators, such as CsI: Tl or LaBr₃: Ce, are always limited by hygroscopicity or/and long decay time (>20 ns),[6, 7] while BaF₂ with short decay time (<1 ns) suffers from extra-low light yield due to the forbidden core-valence transitions.

Metal halide perovskite nanocrystals (PNCs) have emerged as a suitable choice for X-ray fast scintillator.[4, 8, 9] The constituting atoms including heavy metal elements can effectively attenuate the incoming X-ray as X-ray absorption cross section increases with the increased atomic number.[10] Specially, PNCs with direct-bandgap show strong oscillator strength of the transition and excitons confinement, bringing fast emission rates and highly probable strong luminescence.[11, 12] However, the greatest challenge of PNCs is their poor stability against long-time operation. Previous strategies were to encapsulate PNCs in a host material, such as meso-silica, porous zeolite, metal-organic framework (MOF), glass, and polymer matrix to improve the stability.[13-17] However, the products in form of powders show strong light scattering and reduce the optical output efficiency, while the transparent matrix, such as amorphous inorganic or organic glass suffered from lattice mismatch and easy aging under long-time X-ray illumination. Therefore, improving the stability of PNCs not at the expense of their excellent optical properties is a great challenge for PNCs-based scintillators. Some previous works reported CsPbCl₃ NCs embedded crystalline host with wider band-gap energy.[18-21]

Here, we synthesized CsPbBr₃ NCs in a wide band-gap Cs₄PbBr₆ single crystal matrix (PNCs embedded PSC) for efficient light output by using one-step low-temperature solution method. Because of the protection of the SC matrix and the perfect lattice matching, the PNCs embedded PSC show minimized nonradiative recombination and short decay time (12.8 ns). The heat, moisture and radiation stability were greatly improved without any encapsulation. Moreover, by controlling the chemical equilibrium, the self-absorption of PNCs was reduced and the photoluminescent quantum yield (PLQY) was increased to 78.5%, comparable to the CsPbBr₃ NCs in solution. Combined with these essential preconditions of the scintillator, the PNCs embedded PSC exhibited good X-ray response and decay. The light yield was 15,290 photons MeV⁻¹, much higher than the commercial scintillator BGO (8,200 photons MeV⁻¹), and the decay time was shorter than most typical scintillators. Our finding highlights the potential of PNCs embedded PSC for next-generation fast scintillators.

2 Experiment section

Materials: CsBr (99.999%) and PbBr₂ (99.999%) powders were purchased from Aladdin Reagent Ltd. DMF (99.9%) was acquired from Sinopharm. All raw materials were used without any further purification.

Fabrication of PNCs embedded PSC: The PNCs embedded PSC was synthesized by using the controlled cooling method. The solvent was the mixture of DMF and deionized water with the volume ratio of 1:1. 4 mmol CsBr and 1 mmol PbBr₂ powders were dissolved in 10 ml solvent at 100 °C with continuous stirring until the mixed solution was totally clear and transparent. To prevent the volatilization of the solvent, the bottles was sealed by PVC tape. Then the solution was cooled down at the speed of 1 °C h⁻¹ to 72 °C and maintained at this temperature for the growth of the tiny crystals. Then the temperature was cooled to room temperature at the rate of 1 °C h⁻¹ to avoid internal stress generation inside the crystal. The as-grown PNCs embedded PSC were washed by anhydrous isopropanol for three times. The CsBr content could be modified for changing the CsBr/PbBr₂ ratio in the crystals.

Characterization: The XRD patterns were recorded by X-ray diffractometer (X'pert3 powder) with a scanning rate of 10° min⁻¹. High resolution transmission electron microscopy (HRTEM) analysis was performed using an electron microscope (JEOL JEM 2100F). The samples for TEM characterization were prepared by grinding the crystal into powders and dispersed in toluene solvent. The X-ray photoelectron spectra (XPS) was recorded by a spectroscopy (AXIS-ULTRA DLD-600W) with a monochrome Al target. The absorption spectra were recorded using a UV-vis-NIR spectrophotometer (PerkinElmer Lambda 35). The PL spectra excited at 365 nm were measured using a fluorescence spectrophotometer (F-7000, HITACHI) equipped with a xenon lamp as the light source. The absolute PLQYs were obtained by a fluorescence spectrometer (F-7000, HITACHI) equipped with an integrated sphere (C9920-02, Hamamatsu Photonics, Japan) excited at 365 nm from a xenon lamp. The temperature dependent PL spectra were conducted by laser confocal Raman spectrometer (LabRAM HR800) with 325 nm laser as the excitation source.

The radioluminescence was measured using a fluorescence spectrophotometer (FluoMax+, HORIBA) with an Amptek Mini-X tube (Au target, 10 W, Newton Scientific M237) as the X-ray source at 50 keV. To quantify the light yield, the PNCs embedded PSC was placed in a integrating sphere, which was coupling to a Si photo-multiplier (PM) (JSP-TN3050-SMT). The photons produced by radioluminescence were collected, amplified and converted into electric signals by the Si PM. The voltage signals were transferred through a high-speed signal acquisition circuit and read out by an oscilloscope (Keysight DSO-S 054A). The commercial BGO SC scintillator was synchronously tested as a reference. The PNCs embedded PSC and BGO were placed at the same posi-

tion in the integrating sphere to avoid dose rate deviation and light scattering effect. Both the sample and the reference (BGO) were thick enough to ensure complete absorption of the incident X-rays with maximum energy of 50 keV. For scintillation decay measurement, ^{22}Na radioisotope was used as a gamma-ray source (photon energy 511 keV), a photomultiplier tube (PMT, Hamamatsu R9800) and an oscilloscope were used for recording the output waveform of electric signals converted from the scintillation photons. The pulse rise time and the transit time spread (FWHM) of the PMT were 1 ns and 270 ps, respectively. The dose rate of X-rays was adjusted by changing the distance between the sample and the X-ray source and the working current from 10 to 140 μA at a constant voltage (50 keV). The dose rate of the tube was calibrated with an ion chamber dosimeter (Magic Max from IBA DOSIMETRY).

3 Results and discussions

The PNCs embedded PSC samples were synthesized by cooling method in terms of temperature-dependent solubility. The solvent was carefully chosen to balance the solubility of the raw materials. In detail, DMF was used to dissolve PbBr_2 because of the strong interactions between PbBr_2 and DMF, while protic H_2O solvent was used for CsBr . CsBr and PbBr_2 powders with the ratio of 3:1, 4:1 and 5:1 (in mol %), respectively, were added into the mixture of DMF and deionized water at 100 $^\circ\text{C}$ until complete dissolution. As the dissolution process took at least 48 hours, the key strategy to guarantee the validity of the temperature-dependent solubility is to avoid the solvent volatilization. Then the solution was cooled down at the speed of 1 $^\circ\text{C h}^{-1}$ until tiny crystals appeared in the solution. The temperature was then maintained for the growth up of the tiny crystals. The as-prepared crystal is shown in **Figure 1a** with regular and transparent appearance, which was the dominated 0D Cs_4PbBr_6 matrix with the $[\text{PbBr}_6]^{4-}$ octahedron completely isolated by the CsBr bridges. Such structure resulted in preferred formation of Pb vacancies. The nearby isolated $[\text{PbBr}_6]^{4-}$ unites spontaneously connect to each other to form corner shared $[\text{PbBr}_6]^{4-}$ frameworks, giving CsPbBr_3 clusters, as shown in **Figure 1b**. With the growth up of CsPbBr_3 clusters into NCs inside a bulk SC, strong luminescence with short decay time could be realized due the intrinsic properties of PNCs, making it a good scintillator candidate.

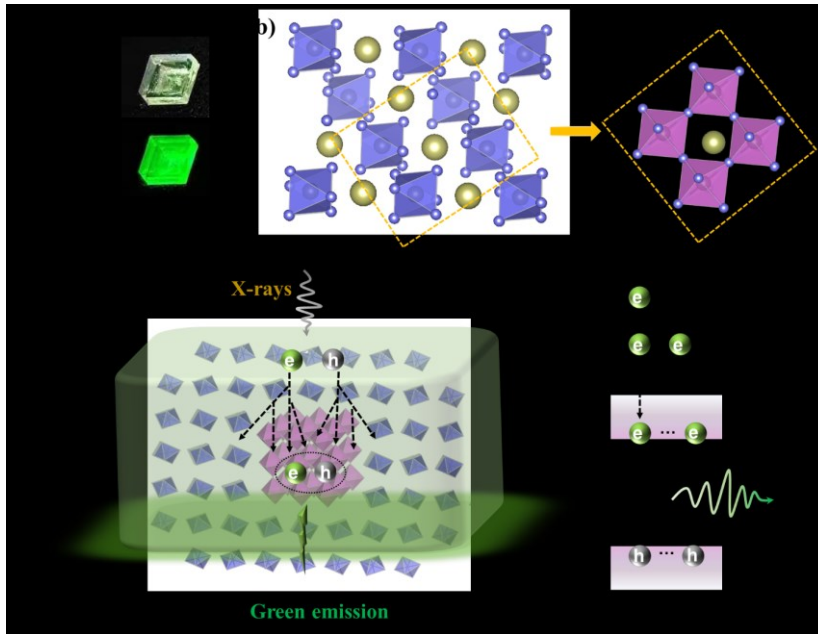


Figure 1: a) Photographs of PNCs embedded PSC irradiated by sunlight (top) and 365 nm-LED (bottom). The size of the crystal was $\sim 8 \text{ mm} \times 8 \text{ mm} \times 3 \text{ mm}$. b) Schematic illustration of structure transformation from 0D isolated $[\text{PbBr}_6]^{4-}$ octahedrons to corner-shared ones. c) Scintillating schematic of PNCs embedded PSC. d) Process of X-ray induced high energy electrons thermally relaxing to generate electron-hole pairs within corner-shared $[\text{PbX}_6]^{4-}$ octahedrons, emitting light and causing scintillation.

The scintillating schematic of PNCs in PSC is depicted in **Figure 1c**. The X-ray photon energy can be partially or completely transferred to electron energy, through photoelectric absorption ($\sigma \propto Z^4/E^3$, where σ is the attenuation coefficient, Z is the effective atomic number and E is the photon energy), Compton scattering ($\sigma \propto Z$) or the electron pair effect. The attenuation coefficient of CsPbBr_3 , Cs_4PbBr_6 and some traditional detection materials towards high-energy photons were calculated according to the photon cross-section database (**Figure S1**).^[22] Regardless of resonant absorption at the K, L and M edges, the absorption of both CsPbBr_3 and Cs_4PbBr_6 was considerable due to their heavy average atomic numbers. The energy of X-rays is captured by the PNCs embedded PSC and produce high energy electrons, such as photoelectrons, Auger electrons and recoil electrons. These hot electrons then relax to produce many low-energy electron-hole pairs *via* coulomb interactions (**Figure 1d**). The electrons are quickly thermalized through interactions with phonons to the conduction of CsPbBr_3 NCs, and generate visible emission by recombination with holes in the valence band. The rest of electron-hole pairs are lost by thermal radiation through electronics-phonons coupling. It should be noted that nonradiative relaxation in SC matrix is smaller than polycrystal matrix or amorphous matrix, due to the reduced grain boundaries.

The structural characterization of PNCs embedded PSC was carried out. As shown in **Figure 2a**, the powder XRD patterns only show dominated Cs_4PbBr_6 phase without characteristic diffraction of CsPbBr_3 , probably due to the low concentration and the small size of CsPbBr_3 NCs. No diffractions peak assigned to CsBr or PbBr_2 was found, indicating no obvious phase separation occurred even with the nonstoichiometric CsPb/PbBr_2 ratios of 3:1 and 5:1. XPS was further applied to survey the PNCs embedded PSC with different CsBr/PbBr_2 ratios. **Figure 2b** and **Figure S2** compare the XPS spectra of the as-grown product with $\text{CsBr/PbBr}_2=4:1$ and 5:1 as well as their corresponding high-resolution spectra of Cs 3d, Pb 4f, and Br 3d. After calibration using the binding energy of C 1s, the binding energy of Cs 3d, Pb 4f, Br 3d was found unchanged. The Br 3d peak from 63-73 eV of PNCs embedded PSC can be fitted by two peaks centered at binding energy of 67.9 eV (I) and 68.7 eV (II), which is similar to the phenomenon reported previously.[23] The observed peak (I) can be attributed to the Br atoms in isolated $[\text{PbBr}_6]^{4-}$ of Cs_4PbBr_6 , while the peak (II) related to the Br atoms in corner-sharing $[\text{PbBr}_6]^{4-}$ of CsPbBr_3 . Furthermore, with increased amount of CsBr, the relative intensity of the peak (II) decreases, revealing a reduced proportion of CsPbBr_3 phase.

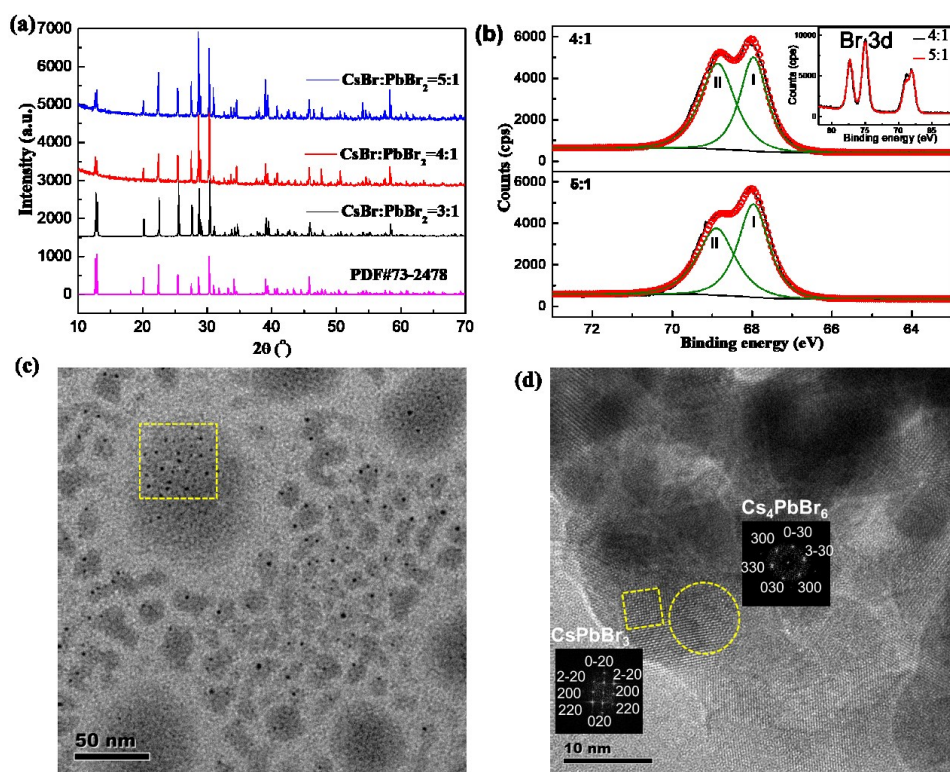


Figure 2: a) XRD patterns and b) Br 3d XPS spectra of PNCs embedded PSC with different CsBr/PbBr_2 ratios. c) TEM and d) HRTEM of PNCs embedded PSC with $\text{CsBr/PbBr}_2=5:1$. The inset of d) is the fast Fourier transform (FFT) images of the two selected areas.

For TEM measurement, the bulk crystal was grinded into small particles with random size distribution and dispersed in toluene as shown in **Figure 2c**. Inside those particles, a few of NCs with a diameter of 3~4 nm can be found, as shown in **Figure S3**. **Figure 2d** shows the enlarged HRTEM image of the squared area selected in **Figure 2c**. The lattice fringes are clearly visible and measurements indicate that the lattice spacing (3.95 Å) mainly corresponded to (300) plane of Cs₄PbBr₆ but with several outliers (2.66 Å) corresponding to (200) plane of CsPbBr₃ (**Figure S4**). For example, the FFT of the squared area in **Figure 2d** matches with the standard diffraction patterns of CsPbBr₃, while the patterns of the surrounding circled area correspond to that of Cs₄PbBr₆. This provides direct evidence for the formation of Cs₄PbBr₆ SCs with embedded CsPbBr₃ NCs in these crystals.

The growth process of CsPbBr₃ NCs in Cs₄PbBr₆ single crystal was monitored by measuring the PL spectra during the cooling crystallization (**Figure 3a**). At the initial stage (tiny crystals), two PL peaks located at 512 nm and 525 nm appear with the former one dominating. With the crystal growing into bulk size, the peak at 512 nm is weakened and the peak at 525 nm become dominating, which may be attributed to the ablation of small NCs into larger ones, resulting in the red-shift of the emission wavelength. NCs inside solid matrix are usually precipitated through *in situ* strategy, depending on the precise control of supersaturation, such as temperature or concentration.[24] The formation enthalpy from Cs₄PbBr₆ to CsPbBr₃ was calculated to be a positive value (0.167 eV) according to the chemical equilibrium $3\text{CsBr} + \text{CsPbBr}_3 \leftrightarrow \text{Cs}_4\text{PbBr}_6$ in this reaction system.[23] This means the transformation from Cs₄PbBr₆ to CsPbBr₃ is not preferred and CsPbBr₃ can exist stably inside Cs₄PbBr₆ matrix from the viewpoint of thermodynamics. Thus, it can be expected that excess CsBr could inhibit the growth of CsPbBr₃ NCs to control the size of CsPbBr₃ NCs in Cs₄PbBr₆ matrix. The absorption and PL spectra of PNCs embedded PSC with different mole ratio of CsBr/PbBr₂ are shown in **Figure 3b**. The strong absorption in the UV region is originated from the wide band gap of Cs₄PbBr₆ crystals (~3.7 eV), while the band-edge absorption and excitonic emission in the visible range is attributed to the embedded CsPbBr₃ NCs. With the increased ratio of CsBr/PbBr₂ from 3:1 to 5:1, the absorption edge and the emission peak are blue shifted, indicating the decreased size of CsPbBr₃ NCs. The self-absorption coefficient (α_s) can be calculated by $\alpha_s = (aI)d\lambda/Id\lambda$, where a is the absorption coefficient, I is the PL intensity, and λ is the wavelength of the overlap between absorption spectra and PL spectra. Thus, the size-dependent self-absorption coefficient decreases from 85.7 cm⁻¹ to 64.2 cm⁻¹ and 25.8 cm⁻¹, resulting in a corresponding sharply increased PLQY from 42.06% to 45.09% and 78.47% (**Figure S5**). When the mole ratio of CsBr/PbBr₂ was further increased to 6:1, the serious phase separation occurred with uneven luminescence, as shown in **Figure S6**. This is because excess CsBr affects the configuration of [PbBr₆]⁴⁻ octahedrons and destroys the stable structure of the crystal.

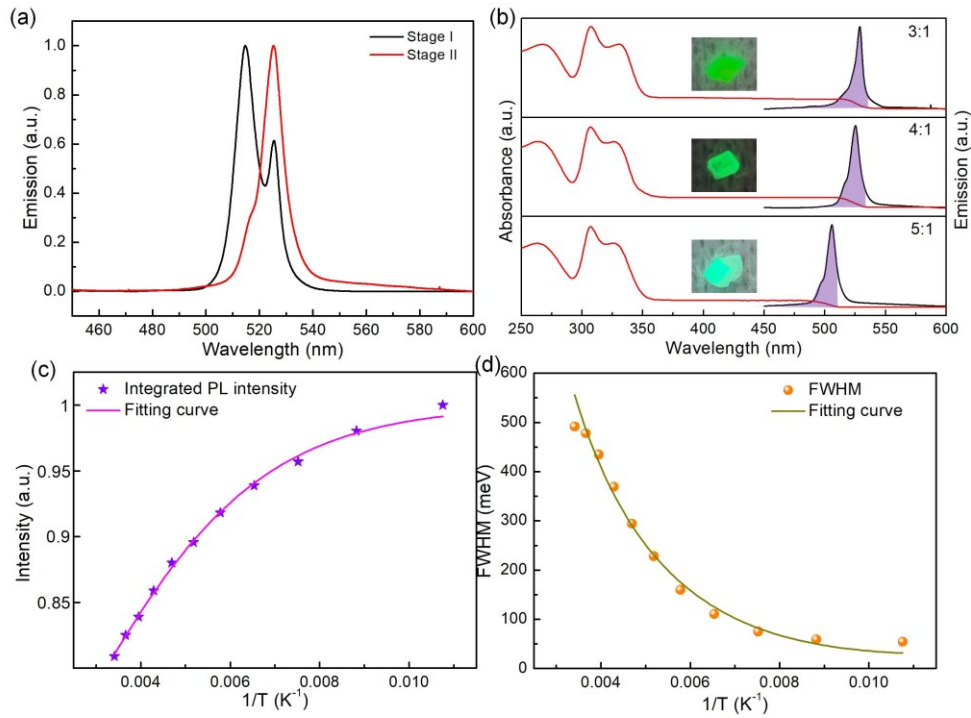


Figure 3: a) Emission evolution of PNCs embedded PSC during the cooling crystallization. b) Normalized absorption and photoluminescence spectra of PNCs embedded PSC with different mole ratio of CsBr/PbBr₂. The inset is the corresponding photo images of the crystals excited by 365 nm LED c) Integral PL intensities of PNCs embedded PSC with CsBr/PbBr₂=5:1 as a function of temperature. Solid line is the simulated curve using Formula (1). d) Full width at half maximum (FWHM) of PL as a function of temperatures. Solid line is the simulated curve using Formula (2).

Further details related to the PL process were explored by the temperature-dependent PL spectra. **Figure 3c** displays the decreased integrated PL intensity with the elevation of the temperature and the fitting curve by the relation

$$I(T) = \frac{I_0}{1 + A \exp[-E_B/(k_B T)]} \quad (1)$$

where T is the temperature, E_B is the activation energy, k_B is the Boltzmann constant and I_0 is the PL intensity at 90 K. Then E_B was calculated to be 40.5 meV, which is the energy required to dissociate the excitons. Although luminescence thermal quenching occurs due to the nature of semiconductors, this phenomenon is reversible. The large activation energy guarantees the impressive emission quality. Assuming that the broadening of the linewidth of the PL peaks is mainly attributed to exciton-phonon interactions, the full width at half maximum (FWHM) as a function of temperature is plotted and fitted by relation[25] (**Figure 3d**)

$$FWHM = \Gamma_0 + \sigma_{ac}T + \frac{\Gamma_{op}}{\exp(\omega_{op}/k_B T) - 1} \quad (2)$$

where Γ_0 (meV) is the FWHM at low temperature levels, σ_{ac} (meV K⁻¹) and Γ_{op} (meV) are the contributions of exciton-acoustic phonon interaction and exciton-optical phonon interaction, respectively, that contribute to the FWHM broadening, and $\hbar\omega_{op}$ (meV) is the optical phonon energy. $\hbar\omega_{op}$ was calculated to be 39.7±1.2 meV, much lower than the displacement of an eigenvector from the Jahn-Teller distortion of the lattice, responsible for the bounded exciton luminescence.[26]. The electron-phonon coupling strength is fitted to be 97.2±5.2 meV, smaller than CsPbBr₃ NCs in solutions and other perovskites with bounded exciton characteristic[27, 28], leading to the minimized non-radiative recombination. Such bounded exciton luminescence and decreased non-radiative recombination are extremely favorable for a fast luminescence decay.

Combined with the good X-ray absorption and excellent emission performance, PNCs embedded PSC is expected to be a competitive scintillator. The scintillation properties were then measured. The radioluminescence spectra of the PNCs embedded PSC with different mole ratio of PbBr₂/CsBr under X-ray (the average energy ~30 keV) excitation are shown in **Figure 4a**. These spectra are consistent with that excited by UV light, revealing the same radiative recombination process. To quantify the light yield, a well-established method was used to count the photons produced by radioluminescence.[29] The PNCs embedded PSC was placed in an integrating sphere, which was coupling to a Si PM. The photons produced by radioluminescence were collected, amplified and converted into electric signals by the Si PM. The voltage signals were transferred through a high-speed signal acquisition circuit and read out by an oscilloscope. The commercial BGO SC scintillator was synchronously tested as a reference. The PNCs embedded PSC and BGO were placed at the same position in the integrating sphere to avoid dose rate deviation and light scattering effect. As shown in **Figure 4b**, with increased mole ratio of CsBr/PbBr₂ in PNCs embedded PSC, the X-ray response increases sharply due to the reduced self-absorption. Using an Amptek Mini-X tube with a working voltage of 50 kV and a current of 50 μA, the average pulse voltage of PNCs embedded PSC and BGO is 0.93 mV (PbBr₂/CsBr=5:1) and 0.57 mV, respectively. The light yield and decay time of commercial BGO was known to be ~8,200 photons MeV⁻¹ and ~300 ns.[30, 31] As the measured voltage response is proportional to the generated photons by X-ray irradiation under identical test conditions, the light yield of PNCs embedded PSC can be obtained by correcting the wavelength-dependent detection efficiency of Si PM, according to formula (3)[29]

$$\frac{LY_{\text{NCinSC}}}{LY_{\text{BGO}}} = \frac{R_{\text{NCinSC}}}{R_{\text{BGO}}} \times \frac{\int I_{\text{BGO}}(\lambda)S(\lambda)d\lambda / \int I_{\text{BGO}}(\lambda)d\lambda}{\int I_{\text{NCinSC}}(\lambda)S(\lambda)d\lambda / \int I_{\text{NCinSC}}(\lambda)d\lambda} \quad (3)$$

where LY is the light yield, R is the corrected response amplitude, $I(\lambda)$ is the radioluminescence intensity, and $S(\lambda)$ is the wavelength dependent detection efficiency. The light yield of PNCs embedded PSC with the CsBr/PbBr₂ ratio of 5:1 was calculated to be 15,290 photons MeV⁻¹, about two times of that for the BGO reference. It should be noted that the light yield of CsPbBr₃ NCs embedded Cs₄PbBr₆ SC is still lower than CsPbBr₃ NCs in solution, due to more non-radiative recombination loss in Cs₄PbBr₆ matrix than organic solvent.[32]

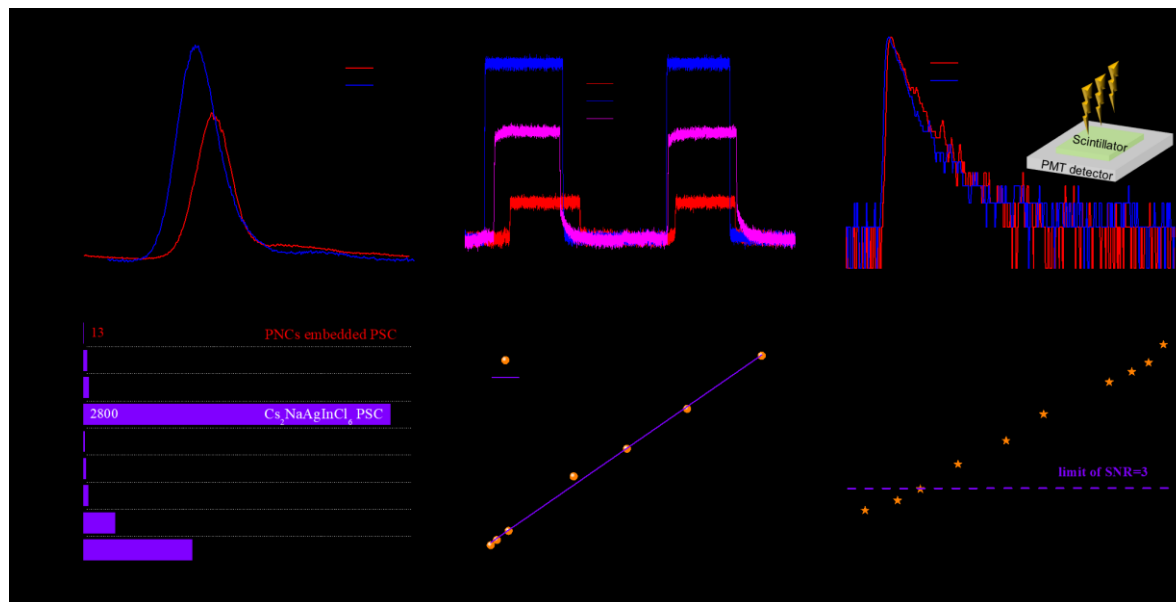


Figure 4: a) Radioluminescence spectra of PNCs embedded PSC with different mole ratio of CsBr/PbBr₂. b) Generated voltage of Si PM by scintillation light of PNCs embedded PSC with commercial BGO single crystal as a comparison. c) Time-resolved radioluminescence decay spectra at room temperature. The excited photon energy was 511 keV generated by ²²Na. d) Comparison of scintillation decay time of PNCs embedded PSC and some typical scintillators. e) Linear X-ray response of PNCs embedded PSC, covering three orders of magnitude from 290 nGy_{air}s⁻¹ to 23.2 μGy_{air}s⁻¹. f) Signal-to-noise ratio value versus the dose rate.

The scintillator decay of PNCs embedded PSC was measured with the excitation of 511 keV γ -ray from ²²Na radiation source, as shown in **Figure 4c**. The average decay time of PNCs embedded PSC was \sim 12.8 ns. Such fast decay time is shorter than almost all the typical scintillators (**Figure 4d**),[4, 33-38] which was attributed to the bounded excitons. The relatively high light yield and a fast emission together give an excellent quality to this composite material as a fast scintillator. It should be noted that CsPbBr₃ NCs in different matrix show various de-

cay time, which is relating to the refraction index of the matrix.[4, 13, 39, 40] More importantly, the cost of PNCs embedded PSC is low attributing to the low-priced raw materials and low-cost solution fabrication process.

Linear response range and signal-to-noise ratio (SNR) are also important features for scintillators. As shown in **Figure 4e**, the PNCs embedded PSC exhibited a linear response towards the dose rate within two orders of magnitude from $290 \text{ nGy}_{\text{air}}\cdot\text{s}^{-1}$ to $23.2 \text{ }\mu\text{Gy}_{\text{air}}\cdot\text{s}^{-1}$, which was enabled by the negligible radiation generated defects. In this range, the radiation dose rate can be predictably correlated to the scintillation response.[41] We then derived the SNR of the PNCs embedded PSC scintillator under various dose rates, as shown in **Figure 4f**. The detection limit fixed at $\text{SNR}=3$ (voltage: 50 kV) is $130 \text{ nGy}_{\text{air}}\cdot\text{s}^{-1}$, which is much lower than the typical medical imaging dose.

For practical applications, the stability of the scintillator should be evaluated. First of all, the as-prepared PNCs embedded PSC was heated at $200 \text{ }^\circ\text{C}$ to check the thermal tolerance. The emission spectrum remained unchanged after 50 h heating (**Figure 5a**), indicating the inhibited structural transformation from Cs_4PbBr_6 to CsPbBr_3 due to the lack of PbBr_2 . Additionally, after being exposed to air at 298 K with a RH of 70% for one month, our PNCs embedded PSC shows only a little reduction of PLQY due to the protection against the hygroscopicity and aggregation nature of the NCs (**Figure 5b**). Above results indicate the good temperature resistance and moisture stability of our PNCs embedded PSC scintillator. Continuous radiation stability is also critical to the signal output of a scintillator. Therefore, we investigated the reliability of the unencapsulated PNCs embedded PSC under working conditions (dose rate $625 \text{ }\mu\text{Gy}\cdot\text{s}^{-1}$). **Figure 5c** shows the response of the PNCs embedded PSC scintillator under on-off X-ray radiation. The response shows negligible degradation throughout the whole test period with an accumulated radiation dose of 324 Gy. The superior radiation stability of the PNCs embedded PSC scintillator is associated with the rigid ionic bonds and with the suppressed electron-phonon interaction as discussed above. These results confirm the enhanced stability of PNCs embedded PSC, which sets a solid foundation for the practical X-ray sensing and imaging application. Therefore, Cs_4PbBr_6 can serve as a protector to improve the stability of the CsPbBr_3 NCs emitter and also ensure efficient light extraction. As for scintillation decay time, it is shorter than that of CsPbBr_3 NCs film scintillator (44.6 ns) due to the larger refraction index of Cs_4PbBr_6 matrix.[4]

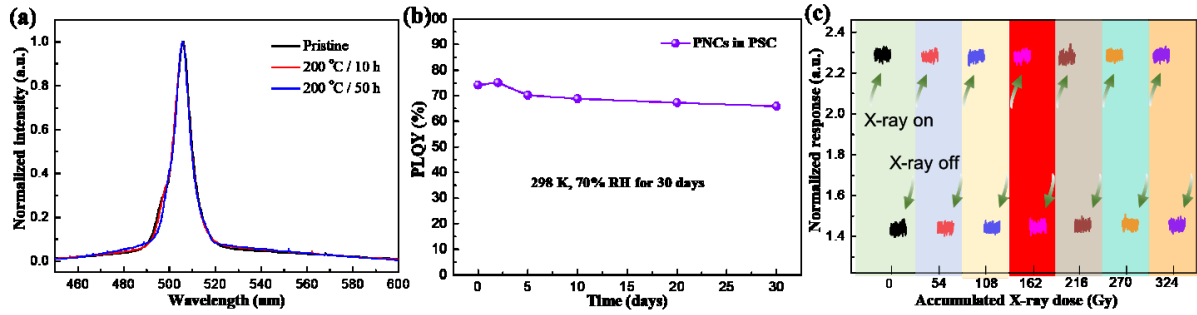


Figure 5: a) Normalized emission spectra of the as-prepared PNCs embedded PSC and that after heating at 200 °C. b) PLQY variation of PNCs embedded PSC excited by 365 nm LED exposed to air atmosphere ($T=298$ K, $RH=70\%$) in one month. c) X-ray response stability of PNCs embedded PSC scintillator detector.

4 Conclusions

In summary, we synthesized CsPbBr_3 NCs in a wide band-gap Cs_4PbBr_6 single crystal matrix (PNCs embedded PSC) for efficient scintillation. The PNCs embedded PSC shows good storage and radiation stability as well as excellent luminescence performance that guarantees a good scintillation response to X-ray signals. The combination of the appreciable light yield ($15,290$ photons MeV^{-1}), the short emission lifetime (12.8 ns), the large detection linearity range and the low detection limit (130 $\text{nGy}_{\text{air}}\cdot\text{s}^{-1}$) as well as potential low-cost, renders our PNCs embedded PSC an highly promising X-ray fast scintillator.

Author contribution: Xia M. was responsible for designing the writing framework and full-text writing. Xu Y., Li X, and Lu P. were responsible for the experiments and manuscript draft. Zhang X. was responsible for the review of the full text.

Acknowledgements

This work is financially supported by National Natural Science Foundation of China (61905082, 61975156), Hubei Natural Science Foundation (2020CFB641) and China Postdoctoral Science Foundation (2021T140234, 2018M642827), State Key Laboratory of Silicate Materials for Architectures (Wuhan University of Technology).

Conflict of interest statement: The authors declare that they have no conflict of interest.

Supplementary Material: Supplementary data associated with this article can be found in the online version

References

- [1] M.J. Yaffe, J.A. Rowlands, X-ray detectors for digital radiography, *Phys. Med. Biol.*, 42 (1997) 1-39.
- [2] W.C. Röntgen, On a new kind of rays, *Science*, 3 (1896) 227-231.
- [3] M. Spahn, X-ray detectors in medical imaging, *Nucl. Instrum. Methods Phys. Res., Sect. A*, 731 (2013) 57-63.
- [4] Q. Chen, J. Wu, X. Ou, B. Huang, J. Almutlaq, A.A. Zhumeckenov, X. Guan, S. Han, L. Liang, Z. Yi, J. Li, X. Xie, Y. Wang, Y. Li, D. Fan, D.B.L. Teh, A.H. All, O.F. Mohammed, O.M. Bakr, T. Wu, M. Bettinelli, H. Yang, W. Huang, X. Liu, All-inorganic perovskite nanocrystal scintillators, *Nature*, 561 (2018) 88-93.
- [5] P. Yang, C.D. Harmon, F.P. Doty, J.A. Ohlhausen, Effect of Humidity on Scintillation Performance in Na and Tl Activated CsI Crystals, *IEEE Trans. Nucl. Sci.*, 61 (2014) 1024-1031.
- [6] I. Mouhti, A. Elanique, M.Y. Messous, A. Benahmed, J.E. McFee, Y. Elgoub, P. Griffith, Characterization of CsI(Tl) and LYSO(Ce) scintillator detectors by measurements and Monte Carlo simulations, *Appl. Radiat. Isot.*, 154 (2019) 108878.
- [7] S. Baccaro, K. Blažek, F. de Notaristefani, P. Maly, J.A. Mares, R. Pani, R. Pellegrini, A. Soluri, Scintillation properties of YAP:Ce, *Nucl. Instrum. Methods Phys. Res., Sect. A*, 361 (1995) 209-215.
- [8] C. Bao, W. Xu, J. Yang, S. Bai, P. Teng, Y. Yang, J. Wang, N. Zhao, W. Zhang, W. Huang, F. Gao, Bidirectional optical signal transmission between two identical devices using perovskite diodes, *Nature Electronics*, 3 (2020) 156-164.
- [9] C.H. Kang, I. Dursun, G. Liu, L. Sinatra, X. Sun, M. Kong, J. Pan, P. Maity, E.N. Ooi, T.K. Ng, O.F. Mohammed, O.M. Bakr, B.S. Ooi, High-speed colour-converting photodetector with all-inorganic CsPbBr₃ perovskite nanocrystals for ultraviolet light communication, *Light Sci Appl*, 8 (2019) 94.
- [10] R.D. Evans, A. Noyau, *The Atomic Nucleus* Vol. 582 (McGraw-Hill, New York, 1955).
- [11] M.A. Becker, R. Vaxenburg, G. Nedelcu, P.C. Sercel, A. Shabaev, M.J. Mehl, J.G. Michopoulos, S.G. Lambrakos, N. Bernstein, J.L. Lyons, T. Stoferle, R.F. Mahrt, M.V. Kovalenko, D.J. Norris, G. Raino, A.L. Efros, Bright triplet excitons in caesium lead halide perovskites, *Nature*, 553 (2018) 189-193.
- [12] F. Hu, H. Zhang, C. Sun, C. Yin, B. Lv, C. Zhang, W.W. Yu, X. Wang, Y. Zhang, M. Xiao, Superior Optical Properties of Perovskite Nanocrystals as Single Photon Emitters, *ACS nano*, 9 (2015) 12410-12416.
- [13] Y. Xu, X. Zhao, M. Xia, X. Zhang, Perovskite nanocrystal doped all-inorganic glass for X-ray scintillators, *J Mater. Chem. C*, 9 (2021) 5452-5459.
- [14] D.N. Dirin, I. Cherniukh, S. Yakunin, Y. Shynkarenko, M.V. Kovalenko, Solution-Grown CsPbBr₃

Perovskite Single Crystals for Photon Detection, *Chem Mater*, 28 (2016) 8470-8474.

[15] J.-Y. Sun, F.T. Rabouw, X.-F. Yang, X.-Y. Huang, X.-P. Jing, S. Ye, Q.-Y. Zhang, Facile Two-Step Synthesis of All-Inorganic Perovskite CsPbX₃ (X = Cl, Br, and I) Zeolite-Y Composite Phosphors for Potential Backlight Display Application, *Adv. Funct. Mater.*, 27 (2017) 1704371.

[16] L.-Y. Wu, Y.-F. Mu, X.-X. Guo, W. Zhang, Z.-M. Zhang, M. Zhang, T.-B. Lu, Encapsulating Perovskite Quantum Dots in Iron-Based Metal–Organic Frameworks (MOFs) for Efficient Photocatalytic CO₂ Reduction, *Angew. Chem. Int. Ed.*, 58 (2019) 9491-9495.

[17] J. Zhang, P. Jiang, Y. Wang, X. Liu, J. Ma, G. Tu, In Situ Synthesis of Ultrastable CsPbBr₃ Perovskite Nanocrystals Coated with Polyimide in a CSTR System, *ACS Appl. Mat. Interfaces*, 12 (2020) 3080-3085.

[18] M. Nikl, K. Nitsch, K. Polak, G.P. Pazzi, P. Fabeni, D.S. Citrin, M. Gurioli, Optical Properties of the Pb²⁺-based Aggregated Phase in a CsCl Host Crystal: Quantum-Confinement Effects, *Phys. Rev. B*, 51 (1995) 5192-5199.

[19] A. Voloshinovskii, S. Myagkota, A. Gloskovskii, S. Zazubovich, Luminescence of CsPbCl₃ Nanocrystals Dispersed in a CsCl Crystal under High-Energy Excitation, *Phys. Status Solidi B*, 225 (2001) 257-264.

[20] A. Voloshinovskii, S. Myagkota, A. Gloskovskii, S. Zazubovich, Luminescence of CsPbCl₃ Microcrystals in CsCl:Pb and PbCl₂:Cs Crystals under Synchrotron Excitation, *Phys. Solid State*, 43 (2001) 1885-1891.

[21] M. Koshimizu, S. Watanabe, K. Shibuya, Y. Muroya, K. Asai, Fast Scintillation Processes in CsCl Crystals Comprising Semiconductor Nanocrystals, *Radiat. Phys. Chem.*, 78 (2009) 1026-1030.

[22] Berger, M. J. et al. XCOM: Photon Cross Sections Database: NIST Standard Reference Database 8 (NIST, 2013); <https://www.nist.gov/pml/xcom-photoncross-sections-database>.

[23] X. Chen, F. Zhang, Y. Ge, L. Shi, S. Huang, J. Tang, Z. Lv, L. Zhang, B. Zou, H. Zhong, Centimeter-Sized Cs₄PbBr₆ Crystals with Embedded CsPbBr₃ Nanocrystals Showing Superior Photoluminescence: Nonstoichiometry Induced Transformation and Light-Emitting Applications, *Adv. Funct. Mater.*, 28 (2018) 1706567.

[24] Y. Ye, W. Zhang, Z. Zhao, J. Wang, C. Liu, Z. Deng, X. Zhao, J. Han, Highly luminescent cesium lead halide perovskite nanocrystals stabilized in glasses for light-emitting applications, *Adv. Opt. Mater.*, 7 (2019) 1801663.

[25] S. Rudin, T.L. Reinecke, B. Segall, Temperature-dependent exciton linewidths in semiconductors, *Phys. Rev. B*, 42 (1990) 11218-11231.

[26] H. Su, Y. Xie, S. Wan, B. Li, Y. Qian, A novel one-step solvothermal route to nanocrystalline CuSbS₂ and Ag₃SbS₃, *Solid State Ionics*, 123 (1999) 319-324.

- [27] W. Zhai, C. Ge, X. Fang, K. Zhang, C. Tian, K. Yuan, S. Sun, Y. Li, W. Chen, G. Ran, Acetone vapour-assisted growth of 2D single-crystalline organic lead halide perovskite microplates and their temperature-enhanced photoluminescence, *RSC Advances*, 8 (2018) 14527-14531.
- [28] Z. Shi, Y. Li, Y. Zhang, Y. Chen, X. Li, D. Wu, T. Xu, C. Shan, G. Du, High-Efficiency and Air-Stable Perovskite Quantum Dots Light-Emitting Diodes with an All-Inorganic Heterostructure, *Nano Lett*, 17 (2017) 313-321.
- [29] B. Yang, L. Yin, G. Niu, J.-H. Yuan, K.-H. Xue, Z. Tan, X.-S. Miao, M. Niu, X. Du, H. Song, E. Lifshitz, J. Tang, Lead-Free Halide Rb_2CuBr_3 as Sensitive X-Ray Scintillator, *Adv. Mater.*, 31 (2019) 1904711.
- [30] J. Gironnet, V.B. Mikhailik, H. Kraus, P. de Marcillac, N. Coron, Scintillation studies of $\text{Bi}_4\text{Ge}_3\text{O}_{12}$ (BGO) down to a temperature of 6K, *Nucl. Instrum. Methods Phys. Res., Sect. A*, 594 (2008) 358-361.
- [31] M. Moszynski, M. Kapusta, M. Mayhugh, D. Wolski, S.O. Flyckt, Absolute light output of scintillators, *IEEE Trans. Nucl. Sci.*, 44 (1997) 1052-1061.
- [32] F. Maddalena, A. Xie, X.Y. Chin, R. Begum, M.E. Witkowski, M. Makowski, B. Mahler, W. Drozdowski, S.V. Springham, R.S. Rawat, N. Mathews, C. Dujardin, M.D. Birowosuto, C. Dang, Deterministic Light Yield, Fast Scintillation, and Microcolumn Structures in Lead Halide Perovskite Nanocrystals, *J. Phys. Chem. C*, 125 (2021) 14082-14088.
- [33] J.T.M.d. Haas, P. Dorenbos, Advances in Yield Calibration of Scintillators, *IEEE Trans. Nucl. Sci.*, 55 (2008) 1086-1092.
- [34] P. Lecoq, Development of new scintillators for medical applications, *Nucl. Instrum. Methods Phys. Res., Sect. A*, 809 (2016) 130-139.
- [35] K. Kamada, T. Endo, K. Tsutumi, T. Yanagida, Y. Fujimoto, A. Fukabori, A. Yoshikawa, J. Pejchal, M. Nikl, Composition Engineering in Cerium-Doped $(\text{Lu,Gd})_3(\text{Ga,Al})_5\text{O}_{12}$ Single-Crystal Scintillators, *Crystal Growth & Design*, 11 (2011) 4484-4490.
- [36] S. Blahuta, A. Bessière, B. Viana, P. Dorenbos, V. Ouspenski, Evidence and Consequences of Ce^{4+} in $\text{LYSO}:\text{Ce,Ca}$ and $\text{LYSO}:\text{Ce,Mg}$ Single Crystals for Medical Imaging Applications, *IEEE Trans. Nucl. Sci.*, 60 (2013) 3134-3141.
- [37] W. Zhu, W. Ma, Y. Su, Z. Chen, X. Chen, Y. Ma, L. Bai, W. Xiao, T. Liu, H. Zhu, X. Liu, H. Liu, X. Liu, Y. Yang, Low-Dose Real-Time X-ray Imaging with Nontoxic Double Perovskite Scintillators, *Light: Sci. Appl.*, 9 (2020) 112.
- [38] W. Pan, B. Yang, G. Niu, K.-H. Xue, X. Du, L. Yin, M. Zhang, H. Wu, X.-S. Miao, J. Tang, Hot-Pressed CsPbBr_3 Quasi-Monocrystalline Film for Sensitive Direct X-ray Detection, *Adv. Mater.*, (2019) 1904405.

- [39] S. Liang, Z. Lu, X. Ding, J. Li, B. Yu, Perovskite Liquid Quantum Dots as a Color Converter for LD-based White Lighting System for Visible Light Communication, in 2019 16th China International Forum on Solid State Lighting & 2019 International Forum on Wide Bandgap Semiconductors China (SSLChina: IFWS), 2019.
- [40] P. Lecoq, New Approaches to Improve Timing Resolution in Scintillators, *IEEE Trans. Nucl. Sci.*, 59 (2012) 2313-2318.
- [41] Y.H. Kim, P. Arunkumar, B.Y. Kim, S. Unithrattil, E. Kim, S.-H. Moon, J.Y. Hyun, K.H. Kim, D. Lee, J.-S. Lee, W.B. Im, A zero-thermal-quenching phosphor, *Nat. Mater.*, 16 (2017) 543-550.